J Sol-Gel Sci Technol (2017) 81:195–204
DOI 10.1007/s10971-016-4185-y

ORIGINAL PAPER: MODELLING, COMPUTATIONAL TOOLS AND THEORETICAL STUDIES OF SOL-GEL AND HYBRID MATERIALS

Validation of the COMPASS force field for complex inorganic–organic hybrid polymers

Thomas S. Asche[1] · Peter Behrens[1] · Andreas M. Schneider[1]

Received: 1 June 2016 / Accepted: 10 August 2016 / Published online: 15 September 2016

Abstract Inorganic–organic hybrid polymers are promising alternatives to simple organic polymers. They combine the advantages of organic and inorganic components in one homogeneous material, which can be adjusted to match sophisticated demands for various possible applications ranging from soft silicones to hard hybrid ceramics. Typically, the inorganic network is formed by a sol-gel reaction whereas the organic network is built by a polymerization reaction. Due to their complex architecture on a molecular level, it is often impossible to experimentally obtain information on the atomistic structures of such hybrid materials. In this work, we validate the all-atom COMPASS force field for the simulation of such materials on the basis of a simplified test system with (methacryloyloxymethyl)dimethylethoxysilane as a precursor; which has only one functionality for inorganic condensation, building only one defined condensation product in the sol-gel reaction. The force field was validated based on the experimentally determined single crystal structure of this condensation product and the calculation of its glass transition and melting temperatures by molecular dynamics. The prediction of fluid densities was validated on liquids of the precursor and the condensation product. The validated force field is applied to demonstrate the influence of inorganic cross-linking in the resulting polymer on a simplified network model.

Graphical Abstract

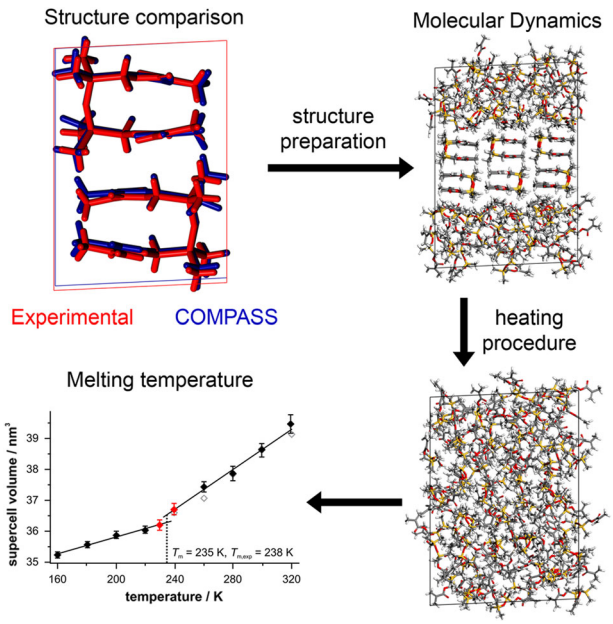

Keywords Ormocer® · Inorganic–organic hybrid polymer · Simulation · Molecular dynamics · Force field validation · Compass

1 Introduction

Inorganic–organic hybrid polymers offer a wide range of tunable properties, e.g. flexibility, hardness, refractive index, and polymerization shrinkage. The combination of organic and inorganic components on a molecular level leads to class-II hybrid materials [1] which can be tailored

Electronic supplementary material The online version of this article (doi:10.1007/s10971-016-4185-y) contains supplementary material, which is available to authorized users.

✉ Andreas M. Schneider
andreas.schneider@acb.uni-hannover.de

[1] Institut für Anorganische Chemie, Leibniz Universität Hannover, Callinstraße 9, Hannover 30167, Germany

for many possible applications [2, 3]. A special group of such hybrid polymers are the organically modified ceramics (Ormocer®s)[1], developed at the Fraunhofer Institut für Silicatforschung in Würzburg, Germany [4–6]. Ormocer®s are prepared in a two-step procedure: First, polycondensation of silanols or alkoxysilanes leads to a large variety of siloxanes, constituting the so-called resin. This resin can be processed in a radical polymerization initiated either by thermal treatment or irradiation to the polymer [7, 8]. For many Ormocer® materials, a direct patterning of the polymer is possible by UV lithography or multi-photon absorption. The latter technique was presented in 1997 and allows the direct manufacturing of nearly arbitrarily shaped three-dimensional structures by using a simultaneous and non-linear absorption process in the focal volume of a pulsed laser [9]. The spatial resolution depends on the material and can be lower than 100 nm [10–12], suitable for integrated optics [13–15] but large scale applications, e.g. biomedical scaffolds, are also possible [16].

Sol-gel derived materials like the Ormocer® resins are often quite complex on the atomistic scale, resulting in very limited possibilities to experimentally obtain information on the underlying molecular structures. The resulting macroscopic properties on the other hand are often well examined. In order to connect the atomistic structures with observable properties, a computational treatment of these materials seems promising. With regard to the complexity of these materials, force field methods offer a good compromise between atomistic accuracy and computational effort: atoms are represented by hard spheres and are connected by predefined bonds to form molecules, while electronic effects are neglected. In principle it is possible to perform geometry predictions on molecules with 10^4 or more atoms by this approach [17]. However, the modeling of reactions and reaction profiles is not possible directly. A number of different approaches can be used to overcome this major disadvantage, e.g. by using bond order potentials as realized in the force field systems ReaxFF [18] and AIREBO [19]. Nevertheless, these reactive potentials are rarely used in the modeling of polymers [20], aside from studies on the pyrolysis mechanisms [21–24]. First studies on the polycondensation of alkoxysilanes with reactive force fields and their parameterization were published recently by Deetz and Faller and will offer more opportunities for simulations in this field in the future [25–27].

Molecular mechanics calculations allow the investigation of different energetic minima on a potential energy surface. However, it is neither guaranteed that with large systems the global minimum is found, nor that the global minimum (calculated for $T = 0$ K) is the most important one at room temperature. Employing molecular dynamics, the influence of a finite temperature and pressure can be investigated, thus allowing a description of the materials at ambient conditions. For Ormocer®-I, first insights in the molecular structure obtained by molecular mechanics and molecular dynamics techniques were published recently [28]. However, a validation of the molecular dynamics at different temperatures and determination of thermodynamic properties was missing.

The system investigated here differs from conventional sol-gel derived hybrid polymers, which typically consist of an inorganic Si–O–Si backbone and an organic cross-linking of these [5, 29]. Nevertheless, the synthesis procedure is similar: starting from alkoxysilanes or silanols, a sol-gel reaction leads to the polymerizable resin in the first step. The final material is obtained in the second step by a radical polymerization reaction, induced by irradiation or thermal treatment.

In contrast to the previously investigated Ormocer®-I, the system presented in this work contains only one type of precursor, an alkoxysilane with only one hydrolysable group ((methacryloyloxymethyl)dimethylethoxysilane) [28, 30]. Therefore, the resin contains only two compounds: the precursor (monomer, M) and the only possible condensation product (dimer, D), as shown in Fig. 1. This reduces the amount of possible configurations dramatically, making this system a simplified model system. This not only facilitates modeling procedures, but also eases the interpretation of experimental results, for example NMR spectra. This makes the system studied here an ideal candidate for fundamental modeling studies, development of corresponding methods and validation of the used parameters and procedures.

Controlled hydrolysis and condensation of (methacryloyloxymethyl)dimethylethoxysilane leads to a 9:1 mixture

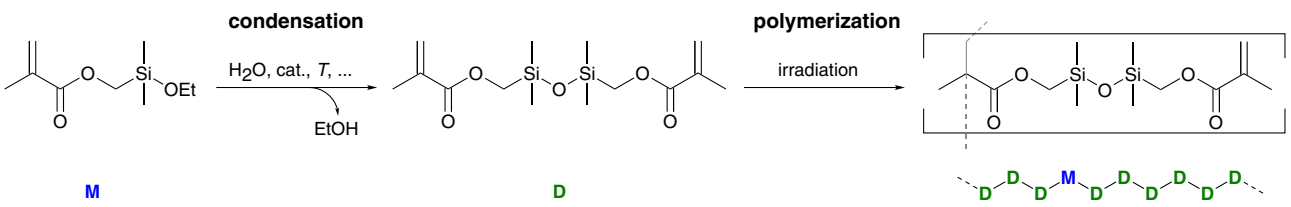

Fig. 1 Reaction scheme for the synthesis of an inorganic–organic hybrid polymer from (methacryloyloxymethyl)dimethylethoxysilane (monomer, M). The ratio of the condensation product 1,3-bis-methacryloyloxymethyl-1,1,3,3-tetramethyldisiloxane (dimer, D) and M in the resin used for polymerization is 9:1, a possible non-cross-linked polymer chain is shown on the *right*

of the D and M compounds in the resin, as estimated by ^{29}Si NMR spectroscopy. Therefore, the resulting polymer is a copolymer built from two different monomers or repeat units. The polymer models in this study precisely reflect the molecular composition of the resin, based on the assumption that all molecules of the resin are part of the final polymer.

As a simple parameter for the quality of the models the experimental and calculated densities at ambient conditions were compared. The calculation of the density via molecular dynamics was validated on the experimental densities of the pure phases of the precursor M and the siloxane D. Afterwards, a series of conjugated polymer models was constructed in order to investigate the influence of inorganic cross-linking in the material, which can occur due to the bifunctional molecules D formed in the condensation reaction. Comparable to other inorganic-organic hybrid polymers, two different polymer chains are connected by inorganic polymer structures, resulting in a cross-linked polymer network. In contrast to organic cross-linked polymers, the organic polymer chains are connected only by inorganic Si–O–Si groups of the cross-linking molecules D.

2 Experimental and methods

2.1 Experimental

The condensation product 1,3-bis-methacryloyloxymethyl-1,1,3,3-tetramethyldisiloxane was synthesized as described by Merker and Scott [31]: 2.04 g (19 mmol) hydroquinone was dissolved under stirring in 85.6 mL (698 mmol) xylol. Successively, 33.8 mL (398 mmol) methacrylic acid, 51.0 mL (368 mmol) triethylamine, and 37.0 mL (168 mmol) bis (chloromethyl)tetramethyldisiloxane were added. The mixture was refluxed for 8 h. The formed precipitate was dispersed in 70 mL xylol. After filtration, fractionated distillation yielded 15 g of 1,3-bis-methacryloyloxymethyl-1,1,3,3-tetramethyldisiloxane.

^{1}H NMR (400 MHz, CCl_3D) δ ppm 0.16 (12 H, s, Si-$(CH_3)_2$), 1.93 (6 H, dd, $J = 1.50$, 0.80 Hz, methacrylate-CH_3), 3.77 (4 H, s, Si-CH_2), 5.52 (2 H, dq, $J = 2.00$, 1.50 Hz, vinyl-H), 6.06 (2 H, dq, $J = 2.00$, 0.80 Hz, vinyl-H) (The full spectrum is available in the Supplementary material.)

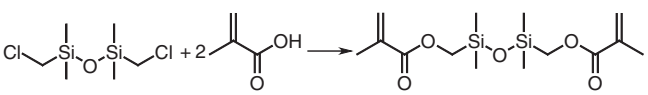

[1] Ormocer® is a registered trademark of Fraunhofer Gesellschaft zur Förderung der Angewandten Forschung e.V., Germany.

Differential scanning calorimetry (DSC) measurements showed a glass transition between −108 and −105 °C, a crystallization point at −65 °C and a melting point at −35 °C (see Supplementary material).

Single crystals for X-ray analysis were grown directly on the Bruker Kappa Apex II four-circle diffractometer equipped with an Oxford Cryosystems 700 Plus cooling device by performing a zone melting process in a 0.2 mm glass capillary: first, seed crystals were generated by cooling the liquid sample to −75 °C, resulting in a crystalline powder. Afterwards, the sample was partially melted by variation of the Kappa-circle of the diffractometer, which brought parts of the sample out of the cold area. Over a few hours, the melted part was returned to the cold area, resulting in a slow crystallization with crystal growth in a preferred direction. This procedure was repeated at −65 °C, resulting in a single crystal with sufficient quality for structure determination. The diffraction data were collected at −80 °C. The structure was solved and refined using SHELX-2013 software [32]. All non-hydrogen atoms were refined freely with anisotropic displacement parameters, while the hydrogen atoms were allowed to ride on the respective carbon atom. The final refinement using all 3267 independent data converged at $R1 = 0.0765$ and w$R2 = 0.2240$ (GooF = 1.065) with no significant features in the final difference Fourier map. Full data of the structure analysis have been deposited at the Cambridge Crystallographic Data Center: CCDC deposition number 1412947.

2.2 Modeling

All calculations were performed using the Materials Studio 7.0 modeling environment by Accelrys [33]. The COMPASS force field [34] (version 2.8) was chosen since polysiloxanes were included in its parameterization [35]. Its general applicability to inorganic–organic hybrid polymers was shown in previous studies on similar compounds [11, 28]. In this work, the direct validation of the force field was performed by comparing modeling results with an experimentally determined crystal structure and by the calculation of phase transition temperatures. The general applicability for the prediction of fluid densities via molecular dynamics [36] as well as the similarity of this work to studies on polyhedral oligomeric silsesquioxane (POSS) containing polymers using COMPASS [37–39] are further support for the choice of this force field.

The COMPASS force field is a class II force field, using the functional form of CFF-type force fields [40, 41]. In contrast to class I force fields, class II force fields use potentials for valence terms which allow for anharmonicity, e.g. in the bond energy. In CFF-type force fields like COMPASS, fourth-degree polynomial functions are used for the bond and angle energy description. Additionally,

bond/bond, bond/angle, bond/torsion, angle/torsion, angle/angle, and angle/angle/torsion cross-terms are added. These cross-terms are especially important for an improved prediction of the vibrational behavior. Non-bond interactions are calculated in the form of Coulomb and van der Waals interactions, the latter using a Lennard–Jones-9-6 potential. This potential features a weaker repulsion in contrast to the commonly used Lennard–Jones-12-6 potential; this is especially important for simulations of condensed phases [34]. The charges for the coulomb interactions are determined based on the force field type of the atoms using an increment system; the charges are kept fixed during the simulation. Hence, COMPASS is a non-polarizable force field. The COMPASS force field was parameterized using ab initio and empirical training sets. The parameterization procedure starts with the ab initio parameterization, beginning with the fitting of the charge parameters and a subsequent fitting of the valence parameters, while the best-guessed van der Waals parameters are retained. After this ab initio parameterization, the valence and van der Waals parameters are optimized in the empirical optimization against a training set of empirical gas phase and liquid phase properties, respectively. A detailed description of the parameterization procedure can be found in [34].

For all calculations, a 15.5 Å cut-off combined with a cubic spline truncation and long range tail correction was used to simplify the calculation of van der Waals interactions. For the Coulomb interactions, an Ewald summation [42] with an accuracy of 10^{-5} kcal mol^{-1} was employed.

The models of fluid phases and non-cross-linked polymers were constructed with the "Amorphous Cell" module, which uses Monte Carlo sampling techniques to generate different starting structures. Energy-minimized in vacuo structures of the molecules M and D were used and put randomly inside a simulation cell under periodic boundary conditions. For the polymer models, the torsions of the backbone were subject to Monte Carlo sampling. Afterwards, all structures were energy minimized and the structure with the lowest potential energy was selected as a starting point for the following calculations.

The prediction of the glass transition temperature was performed with a simulation cell containing 60 molecules of D with a size of approx. 3.2^3 nm^3. For this purpose, it is common to perform molecular dynamics calculations simulating a cooling process [43–46]. The amorphous starting structure was heated to $T = 300$ K for 0.5 ns, divided in equilibration (0.4 ns) and production phase (0.1 ns), each with a timestep of 1 fs in the isothermal–isobaric ensemble (*NpT*) at ambient pressure (0.1 MPa). The Berendsen baro- and thermostat were used to control the pressure and the temperature, respectively. During production phase, the cell volumes of every 100th dynamics step were saved and averaged, and the standard deviation was computed to estimate the uncertainty of the calculation. Subsequently, this procedure was repeated between 280 K and 100 K in 20 K intervals with descending temperature (simulated cooling), each starting from the final frame of the preceding dynamics run.

The model for the prediction of the melting point was built in a procedure similar to the one presented by Watt et al. [46]: A crystalline supercell ($4 \times 3 \times 3$, 72 molecules, $3 \times 3 \times 4$ nm^3) was generated from the experimentally determined crystal structure. In the central region of this supercell (in c-direction), all molecules were constrained to maintain crystallinity. The layers on the top and bottom were able to move and one molecule was removed from each region to facilitate the building of amorphous structures in the following molecular dynamics calculation (canonical (*NVT*) ensemble, 1200 K, 150 ps). The positions of the atoms in the final frame were energy-minimized, first with the crystalline region fixed and finally without any constraints. An image of the starting structure is shown in Fig. 4 on the left. The molecular dynamics for the melting point prediction were performed analogously to the glass transition, differences being only the considered temperature range (160–320 K) and the sequence of the molecular dynamics runs (simulated heating).

In the case of the fluid phases, the molecular dynamics simulations for density prediction can be started directly from the structures generated by "Amorphous Cell". Nevertheless, for the non-cross-linked polymer models, quenched dynamics simulations (10 ps at $T = 800$ K, canonical ensemble) were used to remove unphysical strains from the structure.

After every cross-linking step, these models were first energy minimized and longer quenched dynamics simulations (100 ps) were performed. The structure with the lowest potential energy was used both as a starting point for the molecular dynamics and for the next cross-linking step.

The molecular dynamics simulations for density prediction were performed in the isothermal-isobaric ensemble (*NpT*) at ambient conditions ($T = 298$ K, $p = 0.1$ MPa), both controlled with the Berendsen baro- and thermostat [47]. The simulations lasted 5 ns with a time step of 1 fs, the densities of the latter 2.5 ns were averaged and the standard deviations were calculated.

3 Results and discussion

3.1 Structural aspects

As described in the experimental section, the single crystals were grown directly on the diffractometer. The structure solution revealed a triclinic crystal structure in space group $P\bar{1}$ (2) with one molecule in the asymmetric unit. Both

methacryloyloxymethyl substituents are located on the same side of the molecule, allowing for compact packing. Additional crystallographic data are given in Table 1.

Similar validation calculations based on single crystal structures had already been performed for diphenylsilanediol and octaphenyl-cyclotetrasiloxane [28]. Here, however, the organic groups are more flexible, leading to a shallower energy hyper surface. Therefore, the force field has to meet even higher demands in order to precisely predict molecular structures.

To ensure that the COMPASS force field is suitable for this specific structure, energy minimization calculations were performed starting with the parameters of the experimentally determined single crystal structure. In Fig. 2 a superposition of the energy minimized and the experimental structure is given, revealing a good congruency between both structures. As expected, the lattice parameters are shortened in the energy optimization because thermal effects are neglected. Molecular Dynamics calculations at the temperature of the crystal structure determination ($T = 193$ K) lead to an elongation of all box constants, as shown in Table 1. However, the crystal structure is maintained and no melting is observed.

Although the energy optimization was performed in space group P1, the inversion center is maintained during the calculation. This implies that the crystal structure correlates at least to a local minimum in the energy hyper surface, validating the suitability of the COMPASS force field for this material.

A comparison of the bond lengths and angles obtained by X-ray crystallography and energy minimization calculations, respectively, provides a reasonable estimation of the force field quality. Table 2 gives an overview of the relevant bond lengths for the siloxane groups. The deviations are acceptable (max 0.03 Å for the bond lengths), only the Si–O–Si bonding angle shows a slightly larger discrepancy of 6.3°, consistent with other force field simulations studies

Table 1 Selected crystallographic data for the single crystal structure of D (1,3-bis-methacryloyloxymethyl-1,1,3,3-tetramethyldisiloxane) determined at $T = 193$ K, compared to the energy optimized structure and the cell parameters during 5 ns molecular dynamics at $T = 193$ K

	Experiment ($T = 193$ K)	Energy optimized ($T = 0$ K)		Molecular dynamics[1] ($T = 193$ K)	
	$P-1$ (2)	$P-1$ (2)		$P1$	
a/Å	6.9901 (1)	6.9547	(−0.5 %)	7.055	(+0.9 %)
b/Å	9.9870 (1)	9.8918	(−1.0 %)	10.192	(+2.1 %)
c/Å	14.2292 (1)	13.881	(−2.4 %)	14.240	(+0.1 %)
α/°	86.529 (1)	86.772	(+0.3 %)	84.986	(−1.8 %)
β/°	78.307 (1)	79.582	(+1.6 %)	79.645	(+1.7 %)
γ/°	85.117 (1)	86.781	(+2.0 %)	84.055	(−1.2 %)
V/Å^3	968.24 (2)	936.65	(−3.3 %)	999.427	(+3.2 %)
Z	2				

[1] Molecular Dynamics calculations were performed in a 4 x 3 x 2 supercell without any symmetry constraints. Structures generated in these calculations naturally do not exhibit any symmetry higher than $P1$; the cell parameters were recalculated from the quadrupled, tripled, and doubled cell parameters, respectively.

Table 2 Selected bond lengths and angles from experimental and simulation data

	Experiment ($T = 193$ K)	Energy optimized ($T = 0$ K)	Molecular dynamics ($T = 193$ K)
Angles/°			
Si–O–Si	159.0	152.7	≈151.8
O–Si–CH_2	109.0	108.5	≈109.2
Bond lengths/Å			
Si(1)–CH_2	1.88	1.91	≈1.91
Si(2)–CH_2	1.88	1.91	≈1.91
Si(1)–O	1.61	1.64	≈1.64
Si(2)–O	1.62	1.64	≈1.64

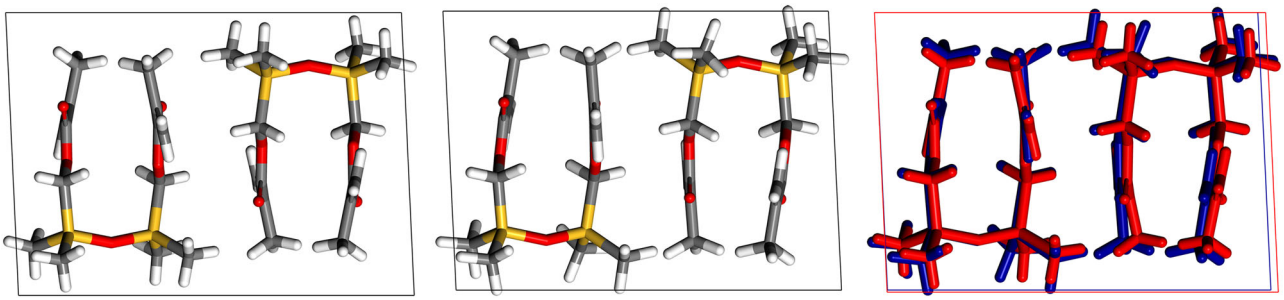

Fig. 2 Comparison of the experimentally determined single crystal structure (*left*) and the energy-optimized crystal structure (*middle*) of 1,3-bis-methacryloyloxymethyl-1,1,3,3-tetramethyldisiloxane (Dimer, D). The superposition of the experimentally determined (*red*) and the energy-optimized (*blue*) structure (*right*) exhibits a good agreement between experimental and simulated structures (all views along the *a*-axis)

on (poly)siloxanes [28]. This is expected, as the change of the Si–O–Si bonding angle does not require a lot of energy, as demonstrated by a number of ab initio calculations on disiloxane [48–50]. Molecular dynamics calculations at the temperature of the structure determination show that the structure (including bonding angles and distances) is preserved even under the influence of thermal energy.

3.2 Prediction of phase transitions

The prediction of phase transitions, e.g. melting point or glass transition, is a key functionality for well parameterized force fields. The COMPASS force field is known to be suitable for the prediction of glass transitions and melting points of several compounds [43–46, 51]. In this case, the prediction is used to ensure the precise scaling of the temperature influence in order to validate all following molecular dynamics calculations at ambient conditions.

3.2.1 Glass transition

As described in the experimental section, the glass transition is calculated by successively cooling a liquid amorphous model of D in a simulation box (approx. 32^3 Å^3) containing 60 molecules with a cooling rate of 20 K/0.5 ns. The volume versus temperature plot is given in Fig. 3. Two domains can be distinguished; each is fitted to a linear model. The intersection of both lines results in the estimated glass transition at 169 K which is in perfect agreement with the experimental value of 168 K.

Compared to common crystallization experiments, the employed cooling rate of 40 K ns^{-1} is orders of magnitude higher. Therefore, a crystallization at a discrete melting point cannot be observed in molecular dynamics simulations with decreasing temperature.

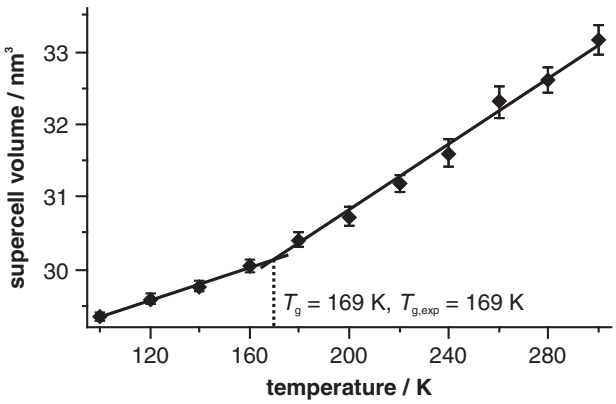

Fig. 3 Supercell volume versus temperature plot for a fully amorphous model with 60 molecules of D during cooling (20 K/0.5 ns). The estimated temperature for the glass transition is 169 K (*dotted line*), the fit curves exhibit R^2 values larger than 0.99

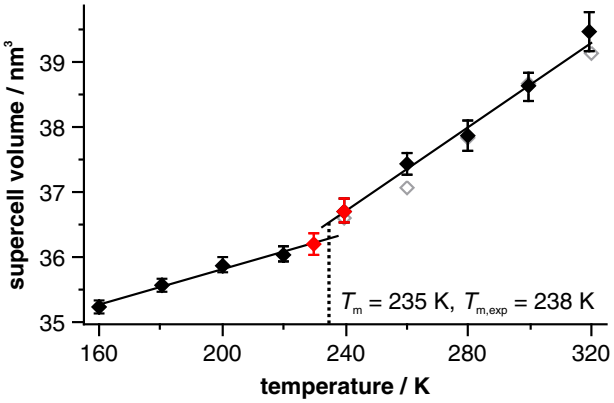

Fig. 5 Supercell volume versus temperature plot for a partially crystalline supercell with 70 molecules of D during temperature increase (20 K/0.5 ns). At 230 and 240 K, the temperature was held for 5 ns (*red diamonds*, see text). The results without holding the temperature at 240 K for 5 ns are shown in *gray open diamonds* for comparison. The *dotted line* depicts the estimated phase transition at $T_m = 235$ K, both fit curves exhibit R^2 values larger than 0.98

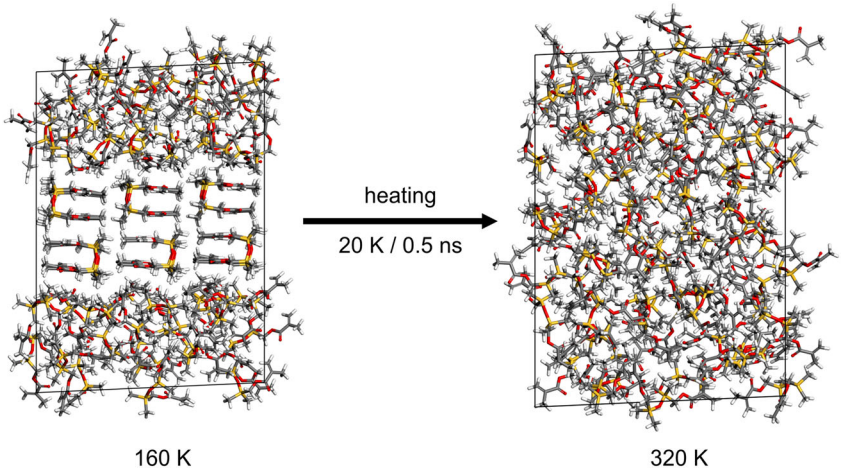

Fig. 4 Model for the melting point prediction of D (*left*: starting point at $T = 160$ K). The molecules in the center of the simulation box were kept fixed during high temperature *NVT* molecular dynamics which were used to generate amorphous regions (liquid phase, *top* and *bottom*). Thus, superheating effects can be reduced as described by Watt et al. [44b]. *right* liquid model at $T = 320$ K obtained by applying the described heating sequence on the *left* model

3.2.2 Melting point

The melting point of D was calculated, as described in detail in the experimental section, in a consecutive series of molecular dynamics calculations, mimicking a heating procedure of a partially crystalline sample. The starting model at $T = 160$ K and the final frame at $T = 320$ K after 4.5 ns of molecular dynamics are shown in Fig. 4. It is clearly visible that a fully amorphous, liquid model is obtained by simulated heating of the ordered structure.

The supercell volume as a function of temperature is shown in Fig. 5. A change of the expansion coefficient is observed at approx. 235 K, close to the experimental melting point of 238 K. Nevertheless, an abrupt increase of the supercell volume cannot be observed, although it would be expected for a first-order phase transition.

Investigating the obtained structure after 240 K, remaining ordered arrangements in the crystalline part can be detected. Because superheating effects were assumed to be involved, extended molecular dynamics calculations (4 ns equilibration and 1 ns production) were performed at 230 and 240 K, each starting from the resulting structure at 220 K. While the crystalline arrangements were preserved at 230 K, a fully amorphous model was obtained at 240 K. From the latter structure, the heating procedure was continued, yielding in the expected expansion behavior of the liquid state and a well-defined step in the supercell volume at the melting point.

However, the calculated increase of the supercell volume at the melting point is comparably small. This can be attributed to two main aspects: First, the investigated structure is only crystalline in a region of 33 % of the volume, therefore the amorphous (liquid) state is present from the beginning of the heating procedure. Second, the specific volume of the crystalline phase is overestimated in all calculations at lower temperatures: molecular dynamics at 193 K starting with the experimentally determined crystal structure or $4 \times 3 \times 2$ supercells exhibit cell volumes which are about 3 % larger compared to single crystal X-ray data, as shown in Table 1.

The results state that the COMPASS force field is suitable for the presented material in general: All investigated properties can be predicted with good reproduction of the experimental values, apart from the proper estimation of the crystalline cell volume at low temperatures. The predicted properties include detailed atomistic features, e.g. bond lengths and bonding angles, as well as macroscopic properties like glass transition and melting point temperatures.

3.3 Validation of the density prediction

Besides the choice of the force field, the size of the simulation cell has a major influence on the predicted density, especially for amorphous materials. Therefore, density calculations on the fluid phases of the system, the precursor M and the resin, were carried out at different cell sizes. Additionally, pure phases of the condensation product D were considered. As shown in Fig. 6, the fluid phases can be described adequately with cells containing more than 500 atoms while enlargement of the cells leads to an increased precision. The overestimation of the density at small cell sizes is not due to an insufficient equilibration, but caused by remaining artificially introduced order in the models.

Another crucial aspect for density prediction is the proper choice of the equilibration procedure, which can become highly demanding for complex polymer systems [54]. In

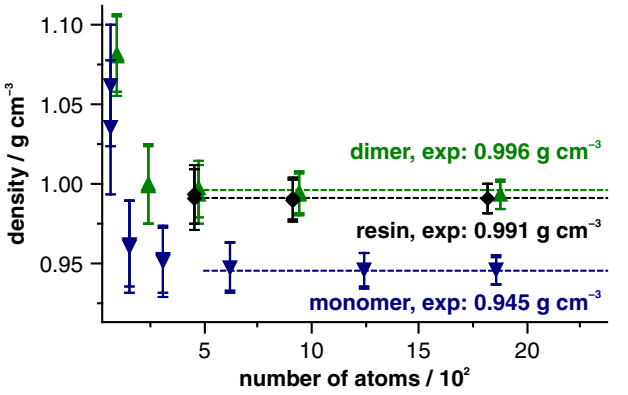

Fig. 6 Densities as obtained from molecular dynamics simulations for fluid phases of M (*blue triangles pointing down*) and D (*green triangles, pointing up*) and the resin (*black diamonds*), a 1:9 mixture of both (see Fig. 1) versus the number of simulated atoms per simulation cell. The experimental densities are given as dotted lines in the corresponding colors [52, 53]. Cells exceeding a size of around 500 atoms reflect the experimental values with standard deviations less than 0.02 g cm^{-3}, at 2000 atoms, the deviations are smaller than 0.01 g cm^{-3}

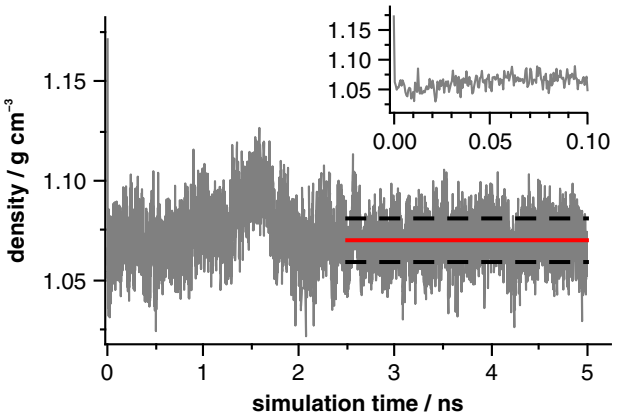

Fig. 7 Typical density plot for a one time cross-linked polymer model with 20 repeat units. The *red solid bar* (2.5–5.0 ns) shows the averaged density (2.5–5.0 ns) while the *black dotted lines* illustrate the estimated standard deviation. In the *inset*, the initial relaxation in the first 100 ps of the simulation is shown

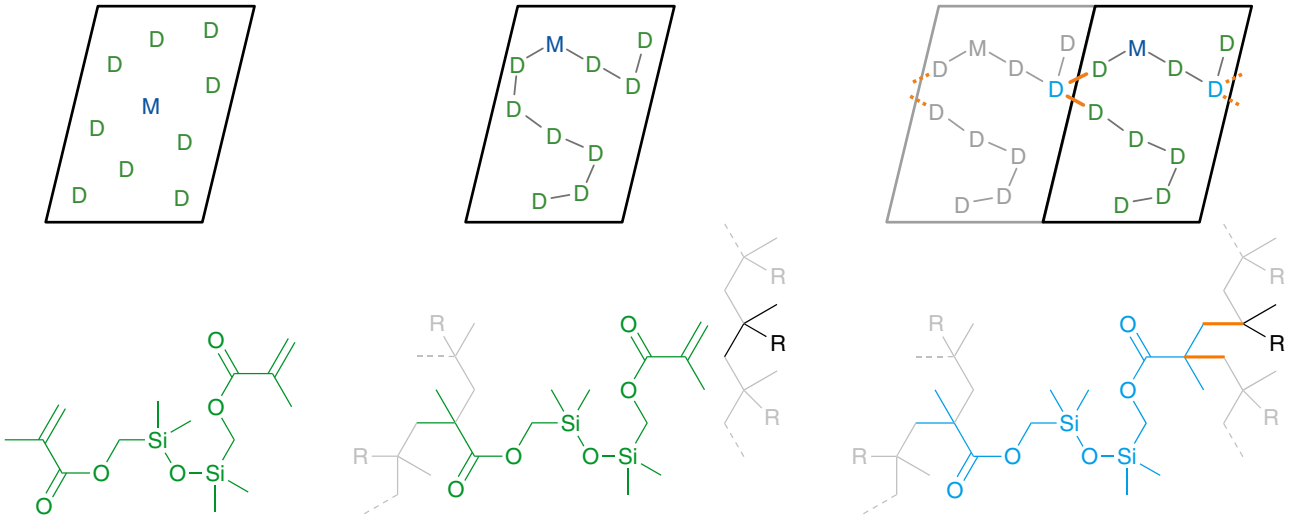

Fig. 8 The three different types of models show schematically the resin with a molar composition of 9:1 (D:M, *top left*), a non-cross-linked polymer chain of the resulting copolymer (*top middle*) and the cross-linked polymer model with one inorganically cross-linking repeat unit (highlighted D in light blue, *top right*). The *orange* bonds are created during the cross-linking procedure while the bond between the two other repeat units is removed. Atomistic descriptions corresponding to the respective models are shown for clarity (*bottom row*)

Fig. 7, the equilibration behavior of a cross-linked polymer model is shown as an example, revealing that an equilibration time of 2.5 ns at ambient conditions leads to stable results and is suitable in our study. Although the main equilibration—recognizable by a volumetric expansion of around 10 %—is observed in the first 100 ps (see inset), longer simulation times are needed to reach equilibrium stage. To keep the calculations consistent, this equilibration time was used for the fluid phases as well.

3.4 Polymer models and inorganic cross-linking

Each polymer model is built up by one individual polymer chain under periodic boundary conditions, as depicted in Fig. 8 (middle). The chain lengths range from ten to hundred precursor units; the ends of the chains were saturated with the fragments of the commonly used initiator Irgacure®-369.

The models presented here are limited to the case of only one polymer chain per asymmetric unit, because of the cross-linking procedure described below. However, an influence on the density prediction could not be detected when models with more than one polymer chain were taken into account (see Fig. 9, red diamonds).

In a first attempt, the non-cross-linked models show steady results for the predicted densities at 1.07 ± 0.01 g cm^{-3}, which is an underestimation of the experimental value of around 4 % (Fig. 9). The increasing chain length, synonymous with the decrease of initiator content at comparable conversion degrees, has no detectable influence on the density, neither has the difference between isotactic, syndiotactic or atactic

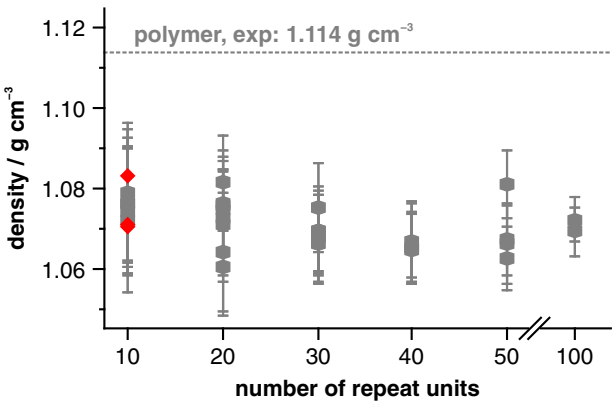

Fig. 9 Densities for single non-cross-linked polymer chains of different lengths obtained from molecular dynamics simulations (*gray hexagons*). For each length, at least two independent models were created. As a comparison, models with four individual chains but same length were created for short chains (*red diamonds*)

polymer configurations. Therefore, the model has to be altered to give a realistic description of the material.

In the non-cross-linked polymer models, only one methacrylate group of each D molecule is part of the polymer structure. When both methacrylate groups are considered as part of the polymer, they can either be part of one chain or cross-link two individual chains. Figure 8 (*right*) illustrates the applied cross-linking procedure: starting from the energy minimized non-cross-linked polymer model (*middle*), the distances from the polymer backbone to all carbon atoms of the unreacted double bonds were measured. All atoms of the original polymer chain belong to the original definition of the cell content: At this

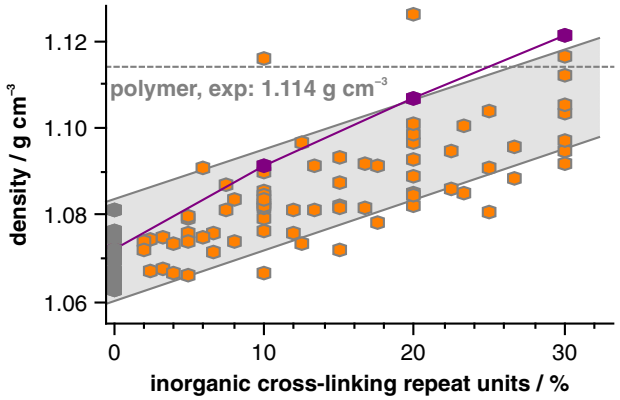

Fig. 10 Densities of cross-linked polymer models (*orange*) in comparison to the non-cross-linked models for chain lengths between ten and fifty repeat units. The connected purple data points are one example of a series of conjugated models for a polymer with ten repeat units in the beginning. The *gray area* illustrates the increase in density, derived from the averaged densities and standard deviations for all models at 0, 10, 20 and 30 % of cross-linking repeat units, respectively

point, only atoms not belonging to the original cell content but originating from the application of periodic boundary conditions were taken into account to ensure the cross-linking connects different polymer chains. For the atoms nearest to the polymer backbone, the two atoms of the previously unreacted double bond were inserted in the polymer chain while the bond between the two outer carbon atoms was removed. As a result of the periodic boundary conditions, a cross-linked polymer network is obtained and not only two connected polymer chains.

In general, the cross-linked models exhibit higher densities in the molecular dynamics simulations, depicted in Fig. 10. The experimental value of the density is reached between 25 and 35 % of inorganically cross-linking repeat units, regardless of the length of the polymer chain. As a result, a highly inorganically cross-linked polymer network is expected to be the main characteristic in the material. The length of the organic polymer backbone cannot be determined, nevertheless it is shown that reasonable results can be obtained at a length of 20–100 carbon atoms.

In some cases—especially for longer chains at a higher degree of cross-linking—the cross-linking procedure as presented may lead to unstable configurations which prevent a proper relaxation of the structure, resulting in an under- or overestimation of the density. These models can be clearly identified in Fig. 10, e.g. the data point at 1.115 g cm^{-3} at 10 % of cross-linking repeat units.

4 Conclusions

In this study, the COMPASS force field is validated for the simulation of inorganic-organic hybrid polymers (ORMOCERs®). Its suitability for the modeling of all stages of the two-step synthesis is shown. The model system used for validation consists of only one alkoxysilane precursor, which forms only one possible siloxane condensation product in the first step. As it represents the main fraction of the resin phase, the condensation product was synthesized in a procedure known from literature [31], allowing to obtain further experimental data and perform additional validation calculations: The experimentally determined single crystal X-ray structure is preserved during energy minimization and molecular dynamics calculations. Additionally, the glass transition and melting point temperatures are predicted and match data from DSC measurements.

Models of the pure phases of the precursor, the condensation product, and the resin are used to determine the minimum size of the simulation cells for first insights into the molecular structure and to gain reliable results concerning the densities. Cells containing more than 500 atoms reflect the experimental densities and allow to distinguish both components, monomers and dimers. However, a higher precision of the density prediction is obtained with larger simulation cells.

The validated force field is used to demonstrate the influence of inorganically cross-linked structures in an inorganic–organic hybrid polymer with a simplified network model. The force field gives reasonable results predicting an increase of the density for a higher degree of inorganic cross-linking. The polymer models contain copolymer chains which reflect the molecular composition of the resin. Models without an inorganic cross-linking between different chains do not lead to a proper description of the material. A series of conjugated models with ascending degree of cross-linking shows the inorganically cross-linking of the polymer to be 25–35 % of the repeat units participating in the cross-linking with an organic backbone length of 20–100 carbon atoms.

The procedure presented reflects the typical synthesis procedure for many inorganic–organic hybrid materials: starting from alkoxysilanes, a resin consisting of siloxanes is obtained in a condensation reaction. This resin is used for the subsequent polymerization, resulting in an organic polymer network which is inorganically cross-linked via the siloxanes.

This validation study shows that comparably small and simple network models can be used to obtain a first insight in molecular structures of inorganic–organic hybrids. The validation of the force field for density prediction gives experimentalists the possibility to perform simulations on similar inorganic-organic hybrid materials, e.g. for modeling studies on the shrinkage behavior during polymerization. If more calculation time is available, larger models employing the COMPASS force

field might be suitable for the prediction of more sophisticated material properties, especially regarding their mechanical behavior.

The presented investigations on the inorganic cross-linking in hybrid polymers can be transferred directly on similar atomistic studies, e.g. other resins containing bifunctional precursors. These are quite common especially in materials for dental applications [55].

Acknowledgments The authors would like to thank Robert Zahn at "Deutsches Institut für Kautschuktechnologie e.V." for the DSC measurements and Dr. Michael Wiebcke and Fabian L. Kempf for assistance in the X-ray single crystal structure determination. The financial support of the Deutsche Forschungsgemeinschaft (DFG) within the priority program 1327 "sub-100 nm structures" is gratefully acknowledged. Individual financial support is granted to Thomas S. Asche by the graduate program MARIO, sponsored by the State of Lower Saxony. S. Steenhusen and R. Houbertz at Fraunhofer Institut für Silicatforschung, Würzburg kindly provided information on the material.

Compliance with ethical standards

Conflict of interest The authors declare that they have no conflict of interests.

References

1. Kickelbick G (2007) Hybrid materials. Synthesis, characterization, and applications, 1st ed. Wiley-VCH Verlag GmbH & Co. KGaA, Weinheim
2. Sanchez C, Belleville P, Popall M, Nicole L (2011) Chem Soc Rev 40:696–753
3. Haas K-H (2000) Adv Eng Mater 2:571–582
4. Schmidt HK (1988) DVS-Berichte 110:54–56
5. Schmidt HK, Popall M (1990) Proc SPIE 1328:249–257
6. Schmidt H, Wolter H (1990) J Non Cryst Solids 121:428–435
7. Haas K-H, Wolter H (1999) Curr Opin Solid State Mater Sci 4:571–580
8. Haas K-H, Rose K (2003) Rev Adv Mater Sci 5:47–52
9. Maruo S, Nakamura O, Kawata S (1997) Opt Lett 22:132–134
10. Burmeister F, Steenhusen S, Houbertz R, Zeitner UD, Nolte S, Tünnermann A (2012) J Laser Appl 24:042014
11. Burmeister F, Steenhusen S, Houbertz R, Asche TS, Nickel J, Nolte S, Tucher N, Josten P, Obel K, Wolter H, Fessel S, Schneider AM, Gärtner K-H, Beck C, Behrens P, Tünnermann A, Walles H (2015) In: A Ostendorf, K König (eds) Optically induced nanostructures. Walter de Gruyter Inc., Berlin
12. Reinhardt C, Ferreras Paz V, Zheng L, Kurselis K, Birr T, Zywietz U, Chichkov B, Frenner K, Osten W (2015) In: A Ostendorf, K König (eds) Optically induced nanostructures. Walter de Gruyter Inc., Berlin
13. Houbertz R, Fröhlich L, Popall M, Streppel U, Dannberg P, Bräuer A, Serbin J, Chichkov BN (2003) Adv Eng Mater 5: 551–555
14. Serbin J, Egbert A, Ostendorf A, Chichkov BN, Houbertz R, Domann G, Schulz J, Cronauer C, Fröhlich L, Popall M (2003) Opt Lett 28:301–303
15. Houbertz R, Domann G, Cronauer C, Schmitt A, Martin H, Park J-U, Fröhlich L, Buestrich R, Popall M, Streppel U, Dannberg P, Wächter C, Bräuer A (2003) Thin Solid Films 442:194–200
16. Stichel T, Hecht B, Houbertz R, Sextl G (2010) J Laser Micro Nanoeng 5:209–212
17. Levine IN (2013) Quantum Chemistry, 7th ed. Pearson Education International, Upper Saddle River
18. van Duin ACT, Dasgupta S, Lorant F, Goddard WA (2001) J Phys Chem A 105:9396–9409
19. Stuart SJ, Tutein AB, Harrison JA (2000) J Chem Phys 112:6472–6486
20. Li C, Strachan A (2015) J Polym Sci Part B Polym Phys 53:103–122
21. Lu X, Wang X, Li Q, Huang X, Han S, Wang G (2015) Polym Degrad Stab 114:72–80
22. Chenoweth K, van Duin ACT, Goddard WA (2008) J Phys Chem A 112:1040–1053
23. Chenoweth K, Cheung S, van Duin ACT, Goddard WA, Kober EM (2005) J Am Chem Soc 127:7192–7202
24. Liu X, Li X, Liu J, Wang Z, Kong B, Gong X, Yang X, Lin W, Guo L (2014) Polym Degrad Stab 104:62–70
25. Deetz JD, Faller R (2014) J Phys Chem B 118:10966–10978
26. Deetz JD, Faller R (2015) Soft Matter 11:6780–6789
27. Deetz JD, Faller R (2015) J Non Cryst Solids 429:183–189
28. Fessel S, Schneider AM, Steenhusen S, Houbertz R, Behrens P (2012) J Sol-Gel Sci Technol 63:356–365
29. Schottner G (2001) Chem Mater 13:3422–3435
30. Buestrich R, Kahlenberg F, Popall M, Dannberg P, Müller-Fiedler R, Rösch O (2001) J Sol-Gel Sci Technol 20:181–186
31. Merker RL, Scott MJ (1961) J Org Chem 26:5180–5182
32. Sheldrick GM (2008) Acta Crystallogr Sect A Found Crystallogr 64:112–122
33. Accelrys Software Inc. (2014) Dassault Systèmes. Materials Studio 7.0. California, USA.
34. Sun H (1998) J Phys Chem B 102:7338–7364
35. Sun H, Rigby D (1997) Spectrochim Acta Part A Mol Biomol Spectrosc 53:1301–1323
36. Rigby D (2004) Fluid Phase Equilib 217:77–87
37. Song X, Sun Y, Wu X, Zeng F (2011) Comput Mater Sci 50:3282–3289
38. Bizet S, Galy J, Gérard J-F (2006) Polymer 47:8219–8227
39. Bharadwaj RK (2000) Polymer 41:7209–7221
40. Maple JR, Hwang M-J, Stockfisch TP, Dinur U, Waldman M, Ewig CS, Hagler AT (1994) J Comput Chem 15:162–182
41. Hwang MJ, Stockfisch TP, Hagler AT (1994) J Am Chem Soc 116:2515–2525
42. Ewald PP (1921) Ann Phys 369:253–287
43. Shiu S-C, Tsai J-L (2014) Compos Part B Eng 56:691–697
44. Wang Z, Lv Q, Chen S, Li C, Sun S, Hu S (2015) Mol Simul 41:1515–1527
45. Sul J-H, Gangadhara Prusty B, Kelly DW (2015) Adv Manuf Polym Compos Sci 1:94–104
46. Watt SW, Chisholm JA, Jones W, Motherwell S (2004) J Chem Phys 121:9565–9573
47. Berendsen HJC, Postma JPM, van Gunsteren WF, DiNola A, Haak JR (1984) J Chem Phys 81:3684–3690
48. Nicholas JB, Winans RE, Harrison RJ, Iton LE, Curtiss LA, Hopfinger AJ (1992) J Phys Chem 96:7958–7965
49. Luke BT (1993) J Phys Chem 97:7505–7510
50. Bär MR, Sauer J (1994) Chem Phys Lett 226:405–412
51. Sun H, Ren P, Fried JR (1998) Comput Theor Polym Sci 8:229–246
52. Merker RL, Noll JE (1956) J Org Chem 21:1537–1539
53. Andrianov KA, Dabagova AK, Syrtsova ZS (1962) Bull Acad Sci USSR Div Chem Sci 11:1487–1491
54. Larsen GS, Lin P, Hart KE, Colina CM (2011) Macromolecules 44:6944–6951
55. Lavigueur C, Zhu XX (2012) RSC Adv 2:59–63